Numerical study of the influence of fluid viscosity on wellbore spalling in drained fractured rock

Jin, W., Zhu, C. and Arson, C.
Georgia Institute of Technology, Atlanta, GA, USA
Pouya, A.
Université Paris-Est, Laboratoire Navier – CERMES, IFSTTAR – Ecole des Ponts Paris Tech, France

ABSTRACT:

The objective of this work is to model the influence of shear stresses induced by viscous fluid flow on wellbore spalling. We simulated a drop of stress and pore pressure at the wall of a meter-scale borehole with a plane strain Finite Element model. The rock mass was modeled as a jointed continuum. Block sliding was predicted from the tangential displacements in the joint after the shear failure criterion was reached. Simulations show that: (1) Higher far field stresses induce more normal stress in the joints, which prevents the occurrence of shear plastic strains in the joints and reduces block sliding at the wall; (2) Shear stresses and consequent shear plastic strains that are induced by viscous fluid flow in the joints are higher for higher fluid viscosities, and decrease over time as the blocks on each side of the joint slide on each other; (3) In joints that are in contact with the borehole, a change of one order of magnitude in the fluid viscosity results in a change in joint shear stress by a factor of 2. Results suggest that if drainage had been simulated over a longer period of time or for a smaller borehole diameter, the failure criterion would have been reached on a larger zone around the borehole, which could have a critical impact on the risk of borehole spalling. The numerical approach proposed in this work is expected to be useful to recommend wellbore operation modes so as to avoid excessive spalling and clogging.

1. INTRODUCTION

Fractures existing prior to, or induced by drilling play a determinant role in spalling and block detachment during the stages of fluid injection and withdrawal in quasi-brittle rocks (e.g., shale). Both numerical simulation and in situ investigation have proved that the mechanical instability resulting in block detachment is affected by the orientation of fractures in reference to the principal direction of in situ stress [1, 2] and to the borehole axis [3, 4]. The fluid pressure difference induced by fluid flow around the borehole - especially in the fractures - also plays a primary role on the stability of blocks [5, 6]. As a matter of fact, the fluid present in the fractures applies a normal force on blocks faces, which disturbs the mechanical equilibrium of these blocks. In addition, viscous fluid flow generates shear stresses on fracture and block faces, which can also affect the mechanical stability of the blocks. To our best knowledge, these shear effects have not been estimated or taken into account in previous studies. The objective of this work is to model the influence of shear stresses induced by viscous fluid flow on wellbore spalling. We model the rock mass as a jointed continuum, in plane strain, with POROFIS Finite Element program [7]. Constitutive laws used for the bulk and joint materials are explained in Section 2. Joint elements are assigned a plastic model coupled to a failure criterion, which allows predicting the relative displacements of the blocks. We simulate a pore pressure drop at the borehole wall. Parametric studies on the ratio far field stress to initial pore pressure and on fluid viscosity are presented in Section 3. Conclusions on the risks of borehole spalling are drawn in Section 4.

2. FINITE ELEMENT MODEL

We designed a plane strain model of jointed rock with POROFIS Finite Element program [7]. We used a one-way coupled algorithm, in which stresses in both the bulk and the joint elements were updated with variations of pore pressures, but fracture aperture and permeability were not updated with stresses.

2.1. Constitutive Laws

We adopted a linear poro-elastic constitutive law for rock bulk elements (i.e., generalized Hooke's law), and an elastic-plastic model for joints, which includes pressure effects. In elasticity, joints are assumed to obey a non-linear hyperbolic law in which the relation between stress and displacement is

$$\begin{aligned} \sigma_t &= k_t u_t + k_{nt} u_n \\ \sigma_n &= k_{tn} u_t + \frac{k_0 u_n}{1 + u_n / e}, \end{aligned} \tag{1}$$

where k_t and k_0 are the tangential stiffness and initial normal stiffness, respectively. The non-diagonal stiffness terms $k_{tn} = k_{nt}$ represent the coupling between normal and shear displacements, which causes dilatancy. e is the initial thickness of the joint, which represents the distance between its two faces when no normal stress applies. When compressive stress increases, the normal stiffness of the joint increases from k_0 to infinity, when the joint is completely closed (Figure 1).

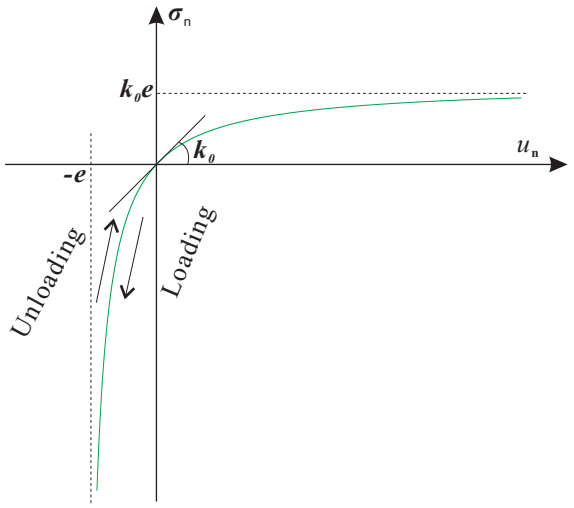

Fig. 1. Non-linear hyperbolic elasticity model for joint normal behavior.

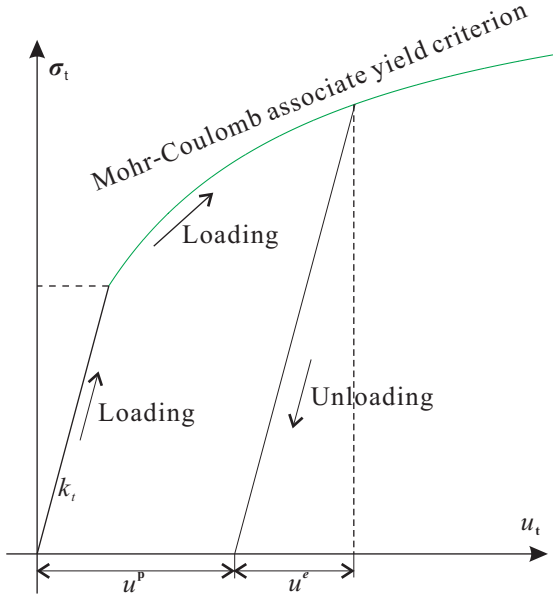

Fig. 2. Elastic-plastic model for joint shear behavior.

Plasticity is assumed to occur when joint shear displacement calculated from Eq. (1) reaches a certain threshold (Figure 2), according to Mohr-Coulomb yield criterion. Plastic displacements are calculated from an associated flow rule:

$$\begin{aligned} \sigma_i &= K_{ij}(u_j - u_j^p) \\ f(\sigma_i) &= |\sigma_t| + \sigma_n \tan\phi - c \le 0 \end{aligned} \tag{2}$$

For the hydraulic analysis, we used Darcy's law with an isotropic permeability for the flow within the rock bulk elements and for the flow along the faces of the joints. We assumed that the conductivity between the bulk and the joints was infinite, i.e. that fluid mass balance was established instantaneously at the rock/joint interface. In the rock bulk elements, fluid velocity is calculated as

$$\boldsymbol{v} = -K\nabla p = -\frac{kg}{\nu}\nabla p, \tag{3}$$

where K is hydraulic conductivity, k is the intrinsic permeability, and ν represents fluid kinematic viscosity. The flow rate inside the joint elements is calculated as

$$q = -c_f \nabla p \tag{4}$$

c_f is the hydraulic conductivity along joint faces (which includes viscosity effects). According to Poiseuille flow model, it is given by the following cubic law:

$$c_f = \frac{(e + u_n)^3 g}{12\nu} \tag{5}$$

where e is the initial fracture aperture and u_n is the normal displacement produced when the joint opens. Eqs. (3-4) govern the fluid flow in steady state. In transient stages, fluid mass transfer is governed by the unconfined homogeneous groundwater flow equation without sink or source, as

$$S\frac{\partial p}{\partial t} = K\Delta p \tag{6}$$

where S is the storage coefficient. After updating the hydraulic variables with Eqs.(3-5) iteratively, the fluid pressure is set equal to the normal stress applied at the joint faces (Figure 3). The viscous shear force induced by fluid flow is calculated from the balance of forces in the joint element, as

$$\tau = \frac{e}{2}\frac{q}{c_f}. \tag{7}$$

The rock mechanical and physical properties adopted in the following simulations are reported in Table 1.

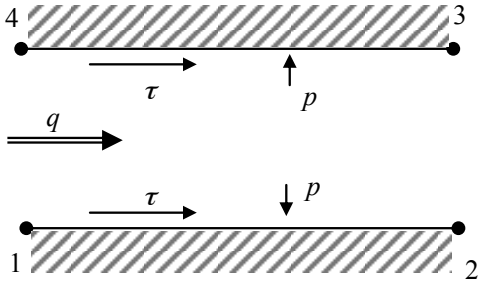

Fig. 3. Mechanical actions of the fluid flow on fractures faces.

Table 1. Mechanical and physical rock properties

	Value	Units
Rock Matrix Properties		
Young's modulus E [8]	60	GPa
Poisson's ratio ν [8]	0.114	-
Intrinsic permeability k_{rock}	1E-12	m^2
Storage coefficient S_{rock}	5E-4	-
Fracture		
Maximum normal stiffness k_0	1000	Gpa/m
Shear stiffness k_t	800	Gpa/m
Coupling stiffness k_{nt}	0	Gpa/m
Initial aperture e	1.0	mm
Cohesion c [9]	2	Mpa
Friction angle ϕ [9]	26.6	°
Intrinsic permeability k_{joint}	1E-7	m^2
Storage coefficient S_{joint}	5E-3	-

2.2. Geometry and Boundary Conditions

We model the cross section of a meter-scale vertical wellbore drilled in a fractured rock mass, in plane strain. Note that in petroleum engineering applications, the size of the borehole would be one order of magnitude smaller (results are interpreted accordingly in the following sections). We calculated the distribution of stress, displacements, pore pressures and flow rates around the borehole, in the domain shown in Figure 4. As indicated by numerous authors, the primary cause of borehole spalling is the presence of joints inside reservoirs prior to fluid injection and withdrawal, especially when these joints intersect the wall of a borehole [1-4]. Since stresses are expected to be higher at the vicinity of borehole wall, we only inserted two sets of quasi-parallel joints within a subdomain of radius 5 m. The two sets of joints were orthogonal and formed an angle of 45 degree with the horizontal. The spacing between joint sets (d_i) was set arbitrarily to an average value of about 60cm.

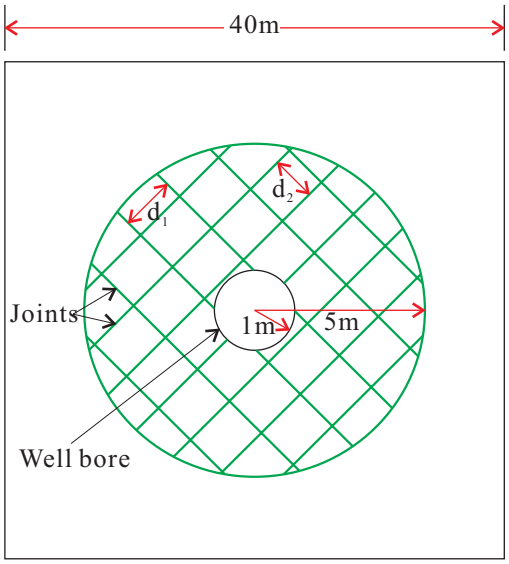

Fig. 4. Finite Element model: geometry and fracture pattern in the rock mass.

It is well known that breakouts grow in the direction of minimum compression, which varies according to the dip directions of joints intersecting the borehole wall [10]. In order to highlight the effect of viscous fluid flow on the development of shear stress in the joints, we assumed that the number, aperture and orientation of the joints were fixed. We assumed that the initial stress at the wall of the borehole was equal to the far field pore pressure p_{inf}. We considered a borehole initially filled with a fluid (which can be used to ensure borehole mechanical stability after excavation). In practice, the density of this fluid, which controls the stress and pore pressure applied at wall of the wellbore, is adjusted so as to avoid excess pore pressure. Accordingly, we set the stress and pore pressure at the wall (σ_{wall} and p_{wall}) equal to the far field pore pressure p_{inf} (Figure 5). In the phase of well production, the fluid used for stability is pumped out of the borehole, and the borehole is filled with gas/oil flowing from the jointed rock to the borehole wall.We fixed the initial pore pressure to 10 MPa and we simulated the pressure drop at the wall in two stages (Figure 5):

1. From Step 1 to Step 2: steady state simulation, with constant pore pressure and time-independent stress drop to the amount of $d\sigma$;
2. From Step 2 to Step 3: transient flow simulation, with a pore pressure drop at the wall, to the amount of $dp = d\sigma = 4\text{MPa}$, over a period of 0.5s.

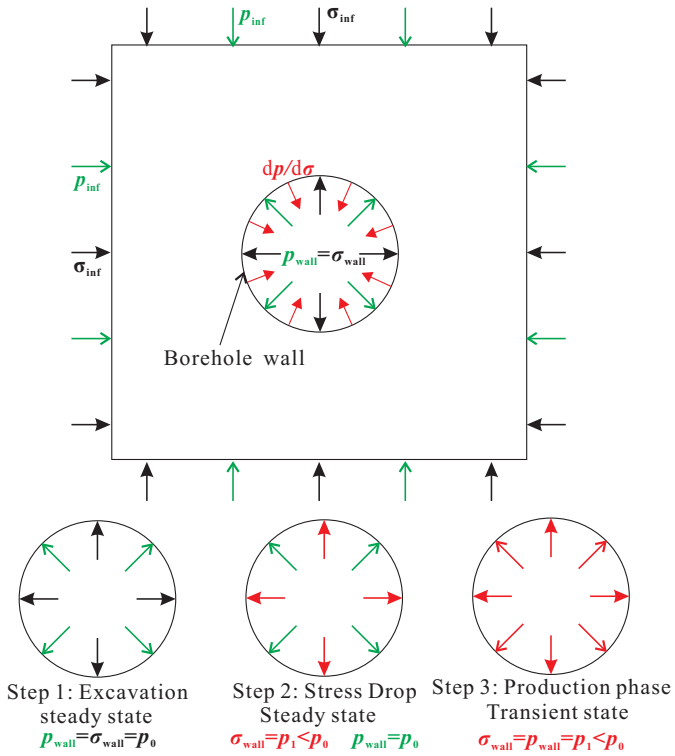

Fig. 5. Boundary conditions adopted in the simulations.

We conducted two sets of parametric studies (Table 2). First, we investigated the effect of the ratio of in situ far field stress over pore pressure. The far field boundary stress varied from 10 MPa to 40 MPa, which corresponds to reservoirs modeled at different depths. Second, we examined the influence of the kinematic viscosity of the fluid on the viscous shear force developed in the joints.

Table 2. Simulation plan for the parametric study

	Case 1	Case 2
Rock Matrix Properties		
In situ stress σ_{inf} / MPa	10, 20, 40	20
Initial pore pressure p_{inf} / MPa	10	10
Pressure drop $\Delta p, \Delta\sigma$ / MPa	4	4
Calculation time period Δt / s	0.5	0.5
Kinematic viscosity ν / mm^2/s	10	1, 10, 100

3. RESULTS AND INTERPRETATIONS

3.1. Redistribution of stress and development of plasticity

The variations of stress induced by a 0.5-second-pore pressure drop are shown in Figure 6 for a far field stress of 40MPa. The fluid kinematic viscosity was 10 mm^2/s, which is equal to that of certain gases (e.g., air), light oil (e.g., motor oil) and glycol. In realistic petroleum engineering problem, the borehole would be 10 times smaller in size. The same mesh could be used to understand how plasticity develops around a borehole during the extraction of hydrocarbons by using a kinematic viscosity 10 to 100 times smaller. This will be discussed in the parametric studies presented in the following.

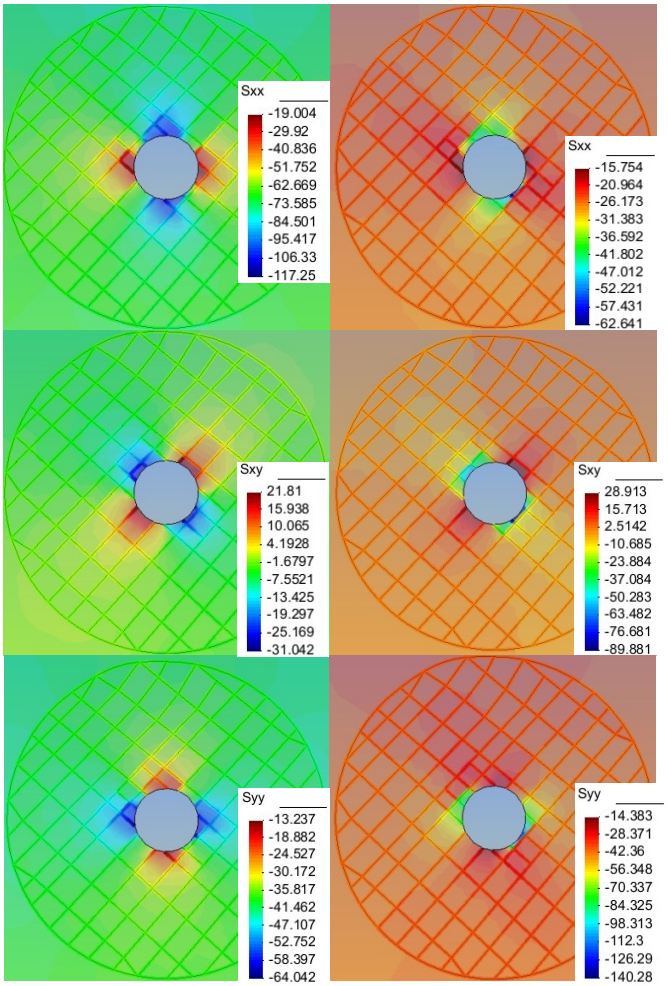

Fig. 6. Comparison of distributions of stress components σ_{xx} (upper), τ_{xy} (middle) and σ_{yy} (Lower) in unit of MPa between Step 1 ($p_{wall} = 10\text{MPa}$) and Step 3 ($p_{wall} = 6\text{MPa}$, t=0.5s). Far field stress: $\sigma_{inf} = 40\text{MPa}$. Fluid kinematic viscosity: $\nu = 10\ \text{mm}^2/\text{s}$. Note: compression was counted negative and tension was counted positive.

After Step 1 (borehole subject to a stress and pore pressure at the wall equal to the pore pressure in the far

field), the elastic distribution of stresses in a *non-fractured* rock mass around the borehole [11] is given by

$$\sigma_{rr} = \sigma_w + (\sigma_\infty - \sigma_w)\left(1 - R^2/r^2\right)$$
$$\sigma_{\theta\theta} = \sigma_w + (\sigma_\infty - \sigma_w)\left(1 + R^2/r^2\right) \quad (8)$$

Where σ_w designates the normal stress at the wall of the borehole and σ_∞ at infinite boundary. Figure 6 shows that the vertical stress at the crown is of the order of $\sigma_{rr} = \sigma_w = 10MPa$ (the pore pressure applied at the wall of the borehole), and that the vertical stress at the sidewalls is about 64MPa, which corresponds to the elastic solution $\sigma_{\theta\theta} = \sigma_w + 2(\sigma_\infty - \sigma_w) = 70\text{MPa}$ with 10% difference which is, of course, due to the presence of fractures. We note that the distribution of stress in the fractured rock mass is not axis-symmetric, due to the non-symmetric fracture pattern.

After the stress (Step 2) and pore pressure (Step 3) drop at the wall, the difference between the compression stresses in the horizontal direction (σ_{xx}) at the crown and at the sidewalls is reduced, whereas that in the vertical direction (σ_{yy}) is enhanced. This result is attributed to the fracture pattern used in this simulation, which controls the magnitude of the displacements in the joints in contact with the wall. In this particular case, drainage generates normal compression (σ_{yy}) and orthoradial tension (σ_{xx}) at the crown.

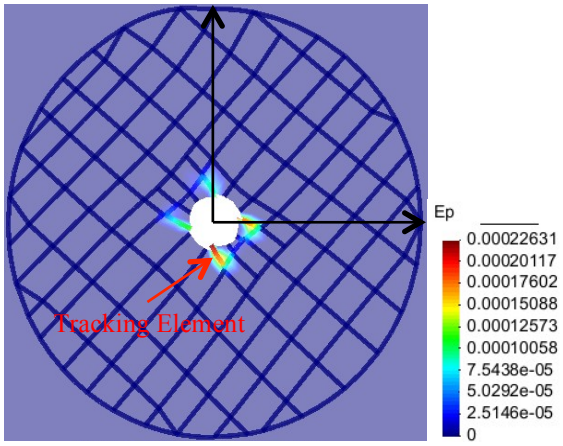

Fig. 7. Shear plasticity strain distribution inside the joints after Step 3 ($p_{wall} = 6\text{MPa}$, t=0.5s). Far field stress: $\sigma_{inf} = 40\text{MPa}$. Fluid kinematic viscosity: $v = 10\ \text{mm}^2/\text{s}$.

In the radial directions that align with the orientation of the joints, the rigid body motion of blocks is free, which induces contact friction and subsequent shear stress both in the joints and in the bulk material. This explains why shear stresses in the bulk are higher in the radial directions that align with the joint directions (Fig. 6). In addition, block sliding and subsequent plastic strains in the joints occur first in the radial direction in which joint spacing is the lowest (Fig. 7).

3.2. Influence of the Far Field Stress

The distributions of horizontal and vertical stresses calculated after Step 3 ($p_{wall} = 6\text{MPa}$, t=0.5s) along the horizontal axis are shown in Figure 8 for the different values of far field stress considered in this parametric study. We verify that the boundary conditions are satisfied in the far field, and the stress distribution far from borehole matches the analytic solution found in elasticity (Eq.8). At the vicinity of the wall of the borehole, fractures slide along interfaces, which induces plastic strains that result in stress softening in that direction. Sliding blocks get compressed, as can be seen from the increase of stress in both x and y directions. Figure 8 illustrates the deviation between the analytical elastic stress distribution and the Finite Element stress predictions as plasticity develops around the borehole.

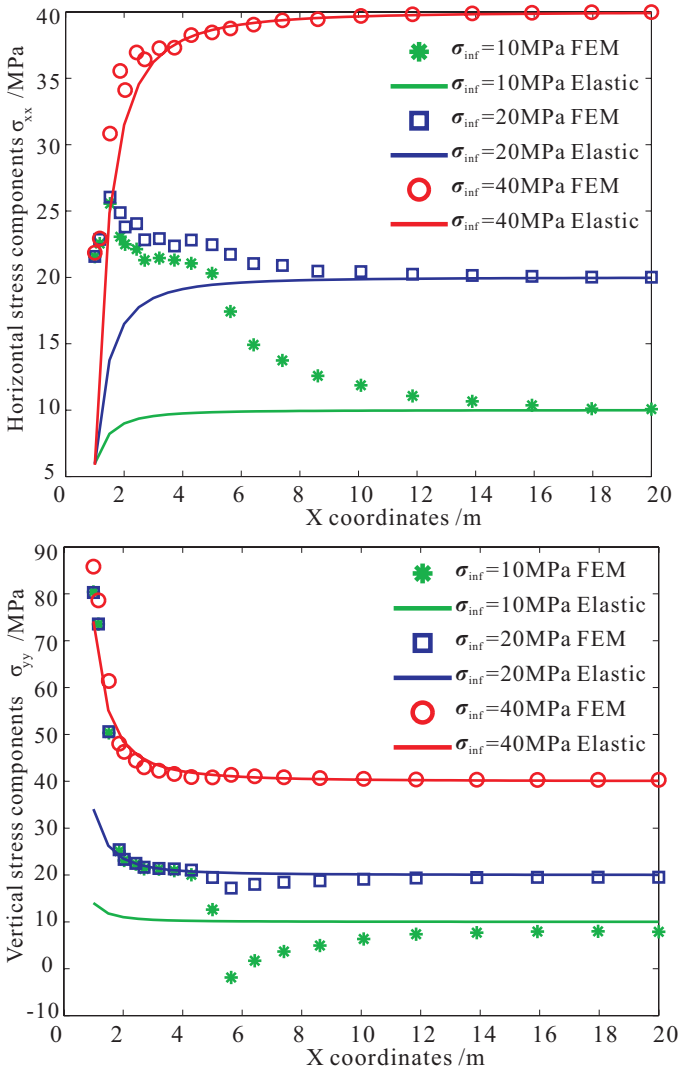

Fig. 8. Horizontal σ_{xx} and vertical σ_{yy} stress distributions along the horizontal line shown in Figure 7 after Step 3 ($p_{wall} = 6\text{MPa}$, t=0.5s). Far field stress: $\sigma_{inf} = 40, 20, 10\text{MPa}$ Fluid kinematic viscosity: $v = 10\ \text{mm}^2/\text{s}$.

Figure 9 shows the influence of the far field stress on the intensity of plastic strain in the tracking joint element

shown in Figure 7. Higher far field stresses induce more confinement, therefore, more normal stress in the joints. According to the failure criterion adopted in the simulations (Eq. (2)), normal stress prevents the occurrence of shear plastic strains in the joints. Therefore, higher the far field stress, lower the plastic strains (Figure 9) and lower the displacements of the blocks at the vicinity of the borehole (Figure 10).

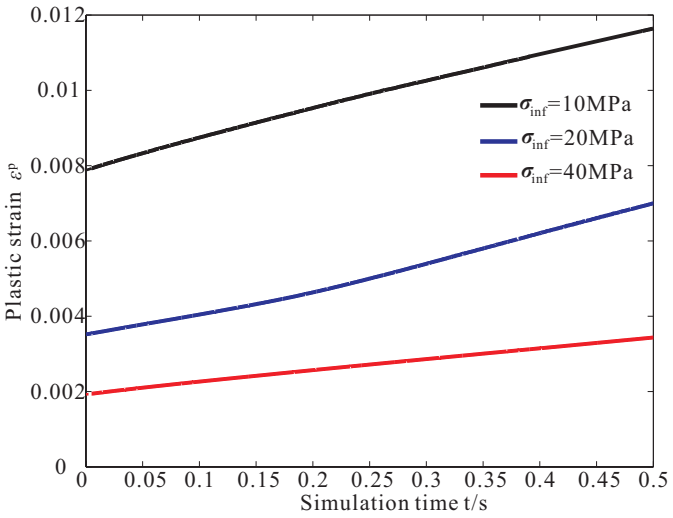

Fig. 9. Plastic strain development at the tracking element shown in Figure 7 after Step 3 ($p_{wall} = 6\text{MPa}$, t=0.5s). Far field stress: $\sigma_{inf} = 40, 20, 10\text{MPa}$. Fluid kinematic viscosity: $v = 10\ \text{mm}^2/\text{s}$.

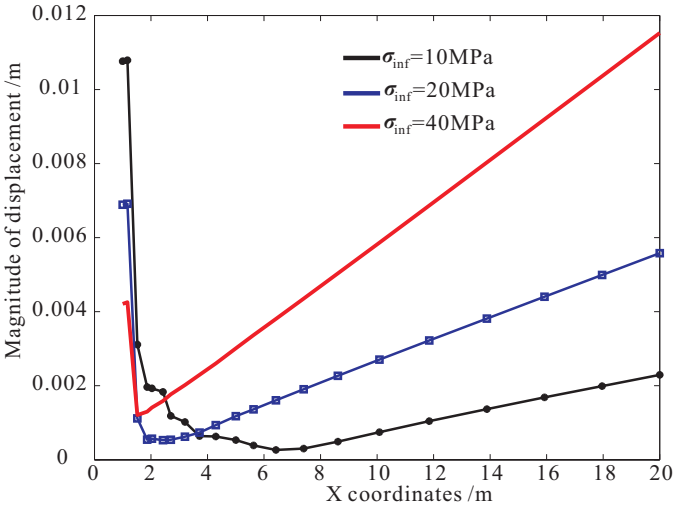

Fig. 10. Norm of the displacement along the horizontal line shown in Figure 7 after Step 3 ($p_{wall} = 6\text{MPa}$, t=0.5s). Far field stress: $\sigma_{inf} = 40, 20, 10\text{MPa}$. Fluid kinematic viscosity: $v = 10\ \text{mm}^2/\text{s}$.

We used a one-way coupled hydro-mechanical algorithm:

- Stresses in the bulk elements were updated with the variations of pore pressure in the joints (from hydraulic equilibrium to mechanical equilibrium);
- Joint aperture (e) was not updated with the variations of mechanical stress in the bulk elements, which implies that the permeability of the joints remained constant during the simulations (from mechanical to hydraulic equilibrium).

According to Eq. (7), the viscous forces in the joints should not depend on the far field stress because we did not account for joint permeability and aperture changes in the simulations. The time evolution of the shear stress in the tracking joint element (Figure 11) confirms this modeling assumption.

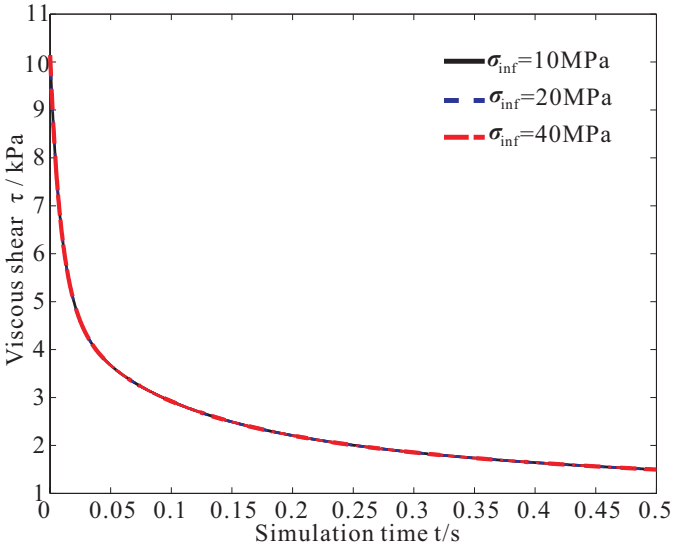

Fig. 11. Viscous shear stress in the tracking joint element shown in Figure 7 after Step 3 ($p_{wall} = 6\text{MPa}$, t=0.5s). Far field stress: $\sigma_{inf} = 40, 20, 10\text{MPa}$. Fluid kinematic viscosity: $v = 10\ \text{mm}^2/\text{s}$.

3.2. Effect of Fluid Viscosity

According to Equations (3) and (4), under a constant pressure gradient, the flow rate in bulk and joint elements is higher for lower fluid viscosities. This modeling assumption is verified in Figure 12. Higher flow rates result in a faster dissipation of excess pore pressure for lower fluid viscosities in both the bulk elements (Figures 13 and 14) and the joint elements. We note that Figure 13 illustrates the difference of permeability between the bulk and the joint materials: the fluid flows from the blocks to the fractures, which represents well the real drainage process. According to

Equations (4) and (6), a faster pore pressure dissipation in the joints reduces the intensity of the viscous shear forces that apply at the fracture faces. Therefore, lower shear stresses develop in the joints for lower fluid viscosities, as shown in Figure 15.

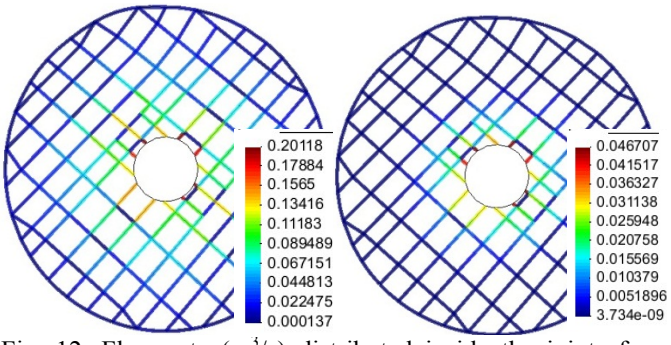

Fig. 12. Flow rate (m^3/s) distributed inside the joints for a kinematic viscosity of $v = 1$ mm^2/s (left) and $v = 10$ mm^2/s (right) after Step 3 ($p_{wall} = 6$MPa, t=0.5s). Far field stress: $\sigma_{inf} = 20$MPa.

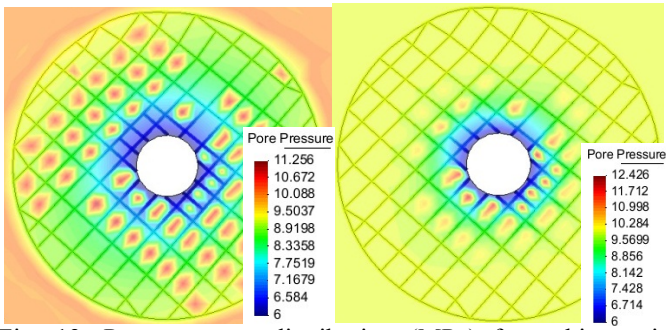

Fig. 13. Pore pressure distribution (MPa) for a kinematic viscosity of $v = 1$ mm^2/s (left) and $v = 10$ mm^2/s (right) after Step 3 ($p_{wall} = 6$MPa, t=0.5s). Far field stress: $\sigma_{inf} = 20$MPa.

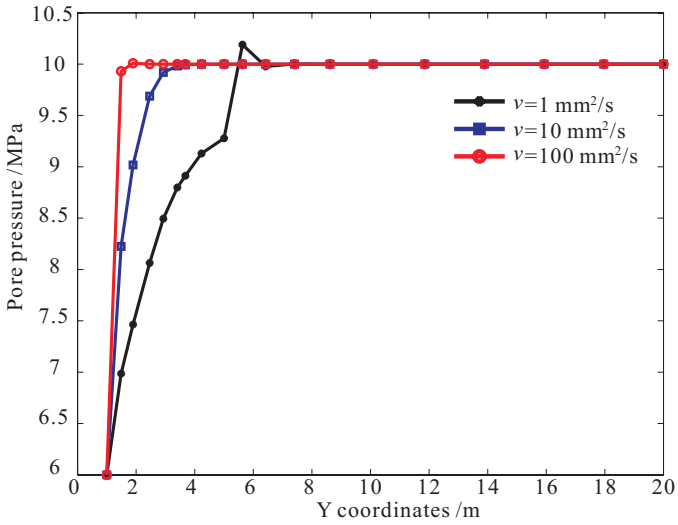

Fig. 14. Pore pressure distribution along the vertical line shown in Figure 7 after Step 3 ($p_{wall} = 6$MPa, t=0.5s). Far field stress: $\sigma_{inf} = 20$MPa. Fluid kinematic viscosity: $v = 1,10,100$ mm^2/s.

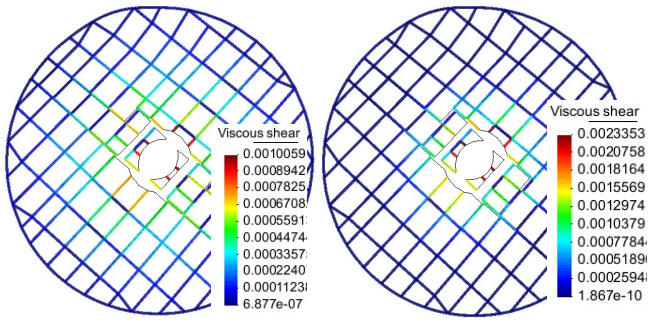

Fig. 15. Viscous shear force (MPa) applied to the joint interface superposed on displacement field (×69) for a kinematic viscosity of $v = 1$ mm^2/s (left) and $v = 10$ mm^2/s (right) after Step 3 ($p_{wall} = 6$MPa, t=0.5s). Far field stress: $\sigma_{inf} = 20$MPa.

We note that the gradient of shear stress in the fractures localizes in a few joint elements close to the borehole. The plots of viscous shear stress in the tracking joint element that is in contact with the wall (in Figure 7) confirm that the shear stress induced by viscous fluid flow in the joints is higher for higher fluid viscosities, and that it decreases over time as the blocks on each side of the joint slide on each other (Figure 16). Correspondingly, plastic shear strains in the joint are higher for higher fluid viscosities, and they increase over time due to block sliding (Figure 17).

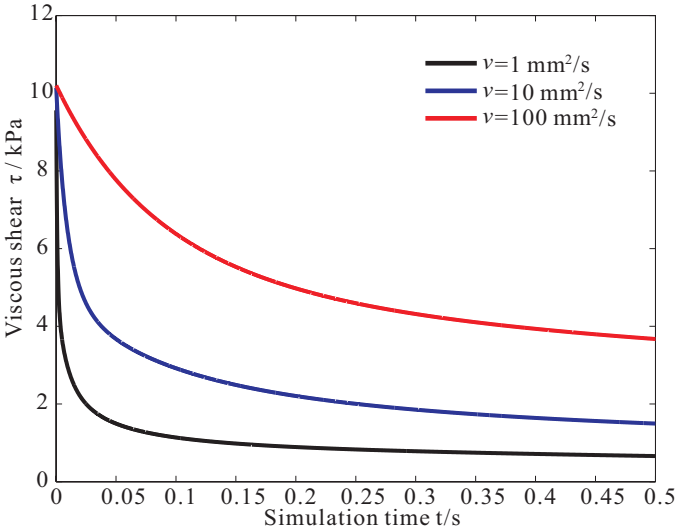

Fig. 16. Viscous shear stress in the tracking joint element shown in Figure 7 after Step 3 ($p_{wall} = 6$MPa, t=0.5s). Far field stress: $\sigma_{inf} = 20$MPa. Fluid kinematic viscosity: $v = 1,10,100$ mm^2/s.

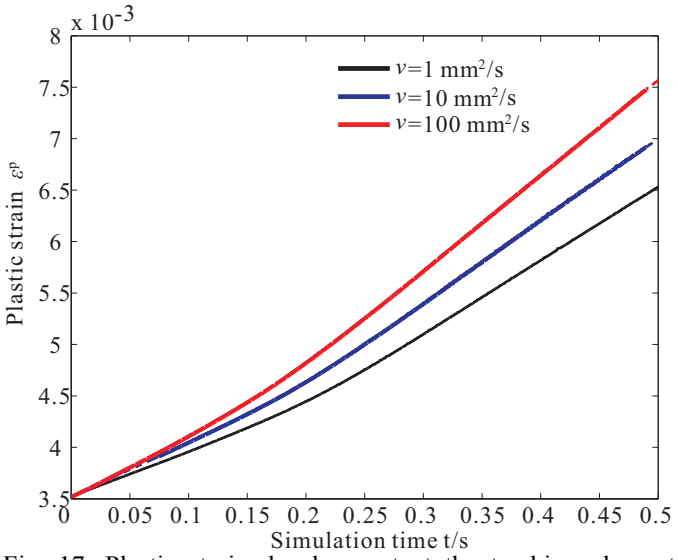

Fig. 17. Plastic strain development at the tracking element shown in Figure 7 after Step 3 ($p_{wall} = 6\text{MPa}$, t=0.5s). Far field stress: $\sigma_{\text{inf}} = 20\text{MPa}$ .Fluid kinematic viscosity: $v = 1,10,100\ \text{mm}^2/\text{s}$.

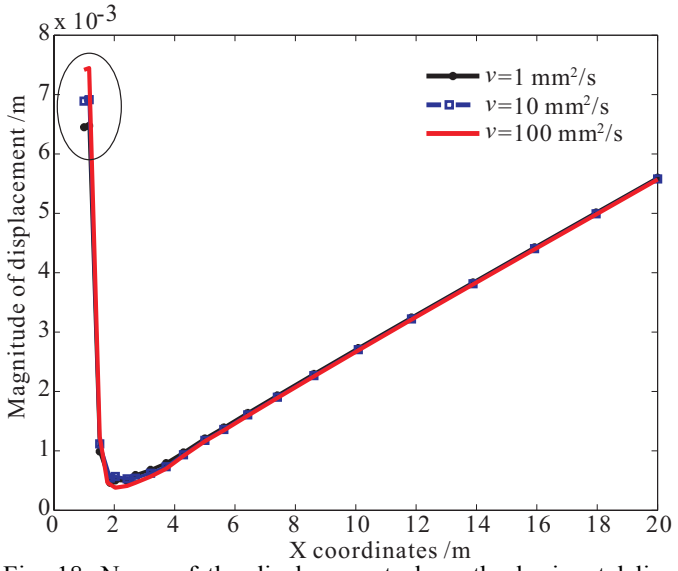

Fig. 18. Norm of the displacement along the horizontal line shown in Figure 7 after Step 3 ($p_{wall} = 6\text{MPa}$, t=0.5s). Far field stress: $\sigma_{\text{inf}} = 20\text{MPa}$ .Fluid kinematic viscosity: $v = 1,10,100\ \text{mm}^2/\text{s}$.

As expected, radial displacements due to block sliding increase with fluid viscosity. But the differences between the three cases simulated are only noticeable close to the cavity wall (Figure 18), because, as noted earlier, joint shear strains localize close to the borehole. As a result, the stress distribution in the bulk of the rock mass is almost the same in the three cases simulated (Figure 19). Nevertheless, we note that a change of one order of magnitude in the fluid viscosity results in a change in joint shear stress by a factor of 2 (Figure 16). This result suggests that if drainage had been simulated over a longer period of time, the failure criterion would have been reached in more than one joint element around the borehole, which could have a critical impact on the risk of borehole spalling.

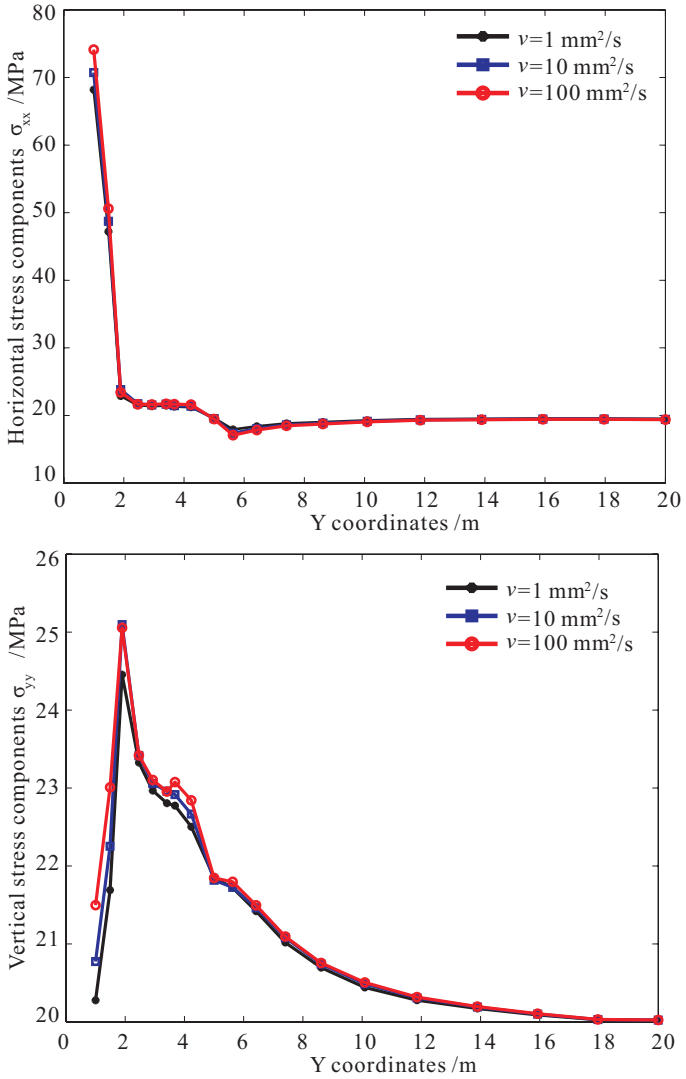

Fig. 19. Horizontal σ_{xx} and vertical σ_{yy} stress distributions along the vertical line shown in Figure 7 after Step 3 ($p_{wall} = 6\text{MPa}$, t=0.5s). Far field stress: $\sigma_{\text{inf}} = 20\text{MPa}$. Fluid kinematic viscosity: $v = 1,10,100\ \text{mm}^2/\text{s}$.

Here, we only simulated the initiation of hydrocarbon extraction over a period of 0.5 seconds to study the stability of the wellbore just after the pressure drop, for a flow of fluid similar to water ($v \approx 1\ \text{mm}^2/\text{s}$), air ($v \approx 10\ \text{mm}^2/\text{s}$), glycol ($v \approx 10\ \text{mm}^2/\text{s}$), light oil ($v \approx 10\ \text{mm}^2/\text{s}$), thick oil ($v \approx 100\ \text{mm}^2/\text{s}$) and slurry with low solid content ($v \approx 100\ \text{mm}^2/\text{s}$). Note that in real petroleum engineering conditions, the size of the borehole would be one order of magnitude smaller. Simulations performed with the mesh employed in this study would have to be repeated with fluid viscosities 10 to 100 times larger to have an insight of borehole stability for the same fluids. Results obtained with a meter-scale borehole with thick oil actually correspond to what would be expected in a petroleum borehole with

water. Higher shear stresses are therefore expected in realistic exploitation conditions. Also note that we simulated drainage at the wall of a borehole with mechanical support. In open hole conditions, even more drag forces are expected. More work is needed to simulate extended periods of transient flow of highly viscous oils and slurries, and to account for changes of fracture permeability upon both withdrawal and injection of fluids into the rock mass.

4. CONCLUSIONS

We simulated a drop of stress and pore pressure at the wall of a meter-scale borehole with a plane strain Finite Element model. The rock mass was modeled as a jointed continuum. Block sliding was predicted from the tangential displacements in the joint after the shear failure criterion was reached. Stress and displacements in the bulk elements were updated with the variations of normal and shear stress in the joints induced by viscous fluid flow. In this exploratory study, joint aperture and permeability were not updated with stress. The main conclusions drawn from the simulations are the following:

1. Higher far field stresses induce more normal stress in the joints, which prevents the occurrence of shear plastic strains in the joints and reduces block sliding at the wall.
2. Shear stress induced by viscous fluid flow in the joints is higher for higher fluid viscosities, and decreases over time as the blocks on each side of the joint slide on each other.
3. Plastic shear strains in the joint are higher for higher fluid viscosities, and they increase over time due to block sliding.
4. Joint shear strains localize close to the borehole.
5. In joints that are in contact with the borehole, a change of one order of magnitude in the fluid viscosity results in a change in joint shear stress by a factor of 2.

Results suggest that if drainage had been simulated over a longer period of time or for realistic borehole sizes (one order of magnitude smaller), the failure criterion would have been reached on a larger zone around the borehole, which could have a critical impact on the risk of borehole spalling. More work is needed to simulate extended periods of transient flow of highly viscous oils and slurries, and to account for changes of fracture permeability upon both withdrawal and injection of fluids into the rock mass. Nevertheless the numerical approach proposed in this work is expected to be useful to recommend wellbore operation modes so as to avoid excessive spalling and clogging.

REFERENCES

1. Willson, S. M., Last, N. C., Zoback, M. D., and Moos, D. 1999. Drilling in South America: a wellbore stability approach for complex geologic conditions. In Latin American and Caribbean petroleum engineering conference. Society of Petroleum Engineers.
2. Santarelli, F. J., Dardeau, C., and Zurdo, C. 1992. Drilling through highly fractured formations: a problem, a model, and a cure. paper SPE, 24592, 4-7.
3. Aadnoy, B., Hareland, G., Kustamsi, A., de Freitas, T., and Hayes, J. 2009. Borehole failure related to bedding plane. In Proceedings of the ARMA conference, Asheville, North Carolina (Vol. 28).
4. Gallant, C., Zhang, J., Wolfe, C. A., Freeman, J., Al-Bazali, T. M., and Reese, M. 2007. Wellbore stability considerations for drilling high-angle wells through finely laminated shale: a case study from Terra Nova. In SPE Annual Technical Conference and Exhibition. Society of Petroleum Engineers.
5. Zhang, X., Last, N., Powrie, W., and Harkness, R. 1999. Numerical modelling of wellbore behavior in fractured rock masses. Journal of Petroleum Science and Engineering, 23(2), 95-115.
6. K. Yamamoto, Y. Shioya, N. Uryu 2002. Discrete element approach for the wellbore instability of laminated and fissured rocks, In SPE/ISRM Rock Mechanics Conference. Society of Petroleum Engineers.
7. Pouya A. (2015) A Finite Element Method for modeling coupled flow and deformation in porous fractured media. International Journal for Numerical and Analytical Methods in Geomechanics, 2015 (submitted)
8. Suárez-Rivera, R., Deenadayalu, C., and Yang, Y. K. 2009. Unlocking the unconventional oil and gas reservoirs: The effect of laminated heterogeneity on wellbore stability and completion of tight gas shale reservoirs. In Offshore Technology Conference, OTC (Vol. 20269).
9. Willson, S. M., Last, N. C., Zoback, M. D., & Moos, D. 1999. Drilling in South America: a wellbore stability approach for complex geologic conditions. In Latin American and Caribbean petroleum engineering conference. Society of Petroleum Engineers.
10. Zoback, M. D., Moos, D., Mastin, L., and Anderson, R. N. 1985. Well bore breakouts and in situ stress. Journal of Geophysical Research: Solid Earth (1978–2012), 90(B7), 5523-5530.
11. Brady, B.H. and Brown, E.T. 2004. *Rock mechanics: for underground mining*. 3rd ed. Dordrecht: Springer Science & Business Media.